The Astrophysical Journal, 1009:62 (17pp), 2026 September 20 https://doi.org/10.3847/1538-4357/ae9d62
© 2026. The Author(s). Published by the American Astronomical Society.
OPEN ACCESS

Stellar Magnetic Storm Induced Magnetospheric Polarity Reversals: A Potential Diagnostic for Distinguishing Unmagnetized and Magnetized (Exo)planets

Sakshi Gupta[1,2,3], Souvik Roy[1,4], and Dibyendu Nandy[1,2,5,6]
[1] Center of Excellence in Space Sciences India, Indian Institute of Science Education and Research Kolkata, Mohanpur 741246, India; dnandi@rri.res.in
[2] Department of Physical Sciences, Indian Institute of Science Education and Research Kolkata, Mohanpur 741246, India
[3] Center for High Energy Systems and Sciences, Defence Research and Development Organization, Hyderabad 500058, India
[4] Department of Atmospheric and Oceanic Sciences, University of California Los Angeles, CA, USA
[5] Raman Research Institute, C. V. Raman Avenue, Sadashivanagar, Bengaluru 560080, Karnataka, India
Received 2026 February 28; revised 2026 August 19; accepted 2026 August 21; published 2026 September 16

Abstract

(Exo)planetary environments are forced by stellar activity, which manifest through variable radiation, particle and magnetic fluxes, stellar winds, flares, and magnetic storms known as coronal mass ejections (CMEs). Recent studies have shown that planets with intrinsic magnetic fields respond differently to stellar wind associated interplanetary magnetic fields (IMFs) compared to planets that lack intrinsic magnetism, as observed in solar system planets. However, detailed investigations that aim to uncover subtle ways in which transient CMEs impact exoplanets are still at a nascent stage. Here, we utilize 3D magnetohydrodynamic simulations to investigate the impact of stellar CMEs on Earth-like (exo)planets with different magnetic fields. Our results, gleaned from 16 different combinations of planetary and IMFs show that planetary atmospheric mass-loss rates are dependent on the relative orientation of stellar wind and planetary magnetic fields, with significantly higher losses when the CME and planetary magnetic fields are oppositely oriented—favoring enhanced magnetic reconnections. In contrast, for unmagnetized planets, the mass-loss rate does not strongly depend on the orientation of the stellar ejecta. We also find that induced magnetospheres in unmagnetized and weakly magnetized planets are prone to global polarity reversals following reversals in the CME-associated stellar wind magnetic field, however, magnetized planets preserve their intrinsic magnetospheric topology. Our analysis of the magnetotail current density dynamics during polarity reversal is qualitatively consistent with observations of Venus. This differential response of induced and intrinsic magnetospheric behavior may provide a potential diagnostic for detecting and characterizing exoplanetary magnetic fields.

Unified Astronomy Thesaurus concepts: Magnetohydrodynamics (1964); Planetary magnetospheres (997); Interplanetary magnetic fields (824); Stellar magnetic fields (1610); Solar magnetic reconnection (1504); Exoplanet atmospheres (487); Stellar coronal mass ejections (1881)

1. Introduction

The variable magnetism of stars and its evolution influence (exo)planetary space environments in ways that have major consequences for planetary space weather and habitability (D. Nandy 2004; D. Nandy & P. Martens 2007; F. Gallet et al. 2017; J. M. Rodríguez-Mozos & A. Moya 2019; I. A. Daglis et al. 2021). In the solar system, coronal mass ejections (CMEs)—energetic ejecta of magnetized plasma from the solar corona—have been extensively studied for decades through direct coronagraphic observations (A. Hundhausen 1999; P. F. Chen 2011). However, our understanding of stellar CMEs on other stars remains limited compared to stellar flare observations.

Stellar flare properties are now well characterized through extensive observations from space-based photometric missions such as Kepler and TESS, which have established flare occurrence rates and energy distributions across a wide range of stellar spectral types (J. R. A. Davenport 2016; H. Yang & J. Liu 2019; M. N. Günther et al. 2020). In contrast, stellar CMEs remain poorly constrained observationally and have been inferred only through indirect signatures such as blueshifted Balmer line asymmetries during superflares (K. Namekata et al. 2022, 2025; S. Inoue et al. 2023), Doppler-shifted X-ray emission lines indicative of erupting cool plasma (C. Argiroffi et al. 2019), and coronal dimming events in far-ultraviolet observations (P. Odert et al. 2017; A. M. Veronig et al. 2025). The magnetic-field orientation of stellar CMEs remains essentially unconstrained observationally, limiting our ability to predict their interaction with (exo)planetary magnetospheres and atmospheres.

These stellar events, analogous to solar CMEs, can be even more energetic in red dwarf stars exhibiting flares much more powerful than those observed on the Sun (A. F. Kowalski et al. 2013). When these energetic plasma ejections propagate through the interplanetary medium and interact with planetary magnetospheres, they are referred to as interplanetary coronal mass ejections (ICMEs) (J. T. Gosling 1993; R. Schwenn 2006). The magnetosphere of an (exo)planet acts as a dynamic shield against the solar–stellar wind and ICMEs, regulating the transfer of energy, mass, and momentum from the stellar wind to the planetary environment (C. T. Russell 2001).

Given these observational constraints on stellar CME properties, a parameter-space study is essential for understanding how stellar CMEs interact with (exo)planetary magnetic fields. Such studies are crucial for determining the

[6] Corresponding author.

Original content from this work may be used under the terms of the Creative Commons Attribution 4.0 licence. Any further distribution of this work must maintain attribution to the author(s) and the title of the work, journal citation and DOI.

evolution of (exo)planetary atmospheres and their potential habitability (H. Lammer et al. 2003; M. L. Khodachenko et al. 2014; O. Cohen et al. 2020; D. Nandy et al. 2023; G. Hazra et al. 2024a).

During stellar CMEs, particle density in the associated shock front, velocity, and the strength of the embedded magnetic field in the stellar wind increases. Thus, when a CME interacts with a planetary atmosphere, it induces significant disturbances that impact atmospheric dynamics (A. Cherenkov et al. 2017). J. D. Alvarado-Gómez et al. (2016) discussed stellar wind conditions in the estimated boundaries of the habitable zones (HZs) of (exo)planet-host stars. For Earth, the magnetosphere's response to ICME impacts can lead to geomagnetic storms characterized by enhanced auroral activity, increased ionospheric currents, and disturbances in the radiation belts (J. W. Dungey 1961; W. D. Gonzalez et al. 1994, 1999). Studies have shown that when the interplanetary magnetic field (IMF) is oriented southward, it is more likely to reconnect with Earth's northward-pointing magnetic field, leading to more intense geomagnetic storms (R. K. Burton et al. 1975; W. D. Gonzalez et al. 1999). This process, known as magnetic reconnection, is a fundamental plasma physics phenomenon that facilitates energy transfer from the solar wind into the Earth's magnetosphere, driving geomagnetic activity (B. U. O. Sonnerup 1974; G. Paschmann et al. 1979; G. R. Burkhart et al. 1990). These geomagnetic storms have far-reaching consequences, like disruptions in satellite operations, communication systems, power grids, as well as increased radiation exposure for astronauts and high-altitude flights (D. N. Baker et al. 1998; T. Pulkkinen 2007; Y. Baruah et al. 2024).

While significant progress has been made in understanding the impact of ICMEs on the Earth's magnetosphere and, to a lesser extent, on other solar system planets, detailed investigations in the context of (exo)planets are just beginning. In a recent work, G. Hazra et al. (2024b) explored the interaction of stellar CMEs in a close-in hot-Jupiter-like system and showed that CME impacts can strongly compress the planetary magnetosphere, modify the global magnetospheric structure, and significantly enhance atmospheric mass-loss rates. However, the response of (exo)planetary environments—spanning unmagnetized, weakly magnetized, and strongly magnetized regimes—remain poorly characterized. Planets that lack a global internal magnetic field, such as Mars and Venus, interact with ICMEs in fundamentally different ways than magnetized planets like Earth.

Therefore, an outstanding challenge in (exo)planetary studies lies in distinguishing planets with and without intrinsic magnetic fields.

Intrinsic magnetospheres arise from a planet's internal magnetic field, providing a dynamically stable magnetic shield against solar–stellar wind interactions (such as in Earth). In contrast, imposed magnetospheres form via the interaction of the stellar wind with the planetary ionosphere in the absence of an intrinsic magnetic field (such as in Mars). The absence of a global magnetic field for these planets means that the ionosphere and atmosphere are directly exposed to stellar wind and energetic particles from stellar flares and ICMEs leading to significant atmospheric erosion (D. Vignes et al. 2000; E. Dubinin et al. 2012; R. Ramstad et al. 2018; A. Basak & D. Nandy 2021). This atmospheric loss, driven by ion pickup and sputtering processes, has profound implications for the long-term evolution of planetary atmospheres (J. G. Luhmann et al. 1992; B. M. Jakosky & R. J. Phillips 2001; H. Lammer et al. 2008).

Understanding the difference between imposed and intrinsic magnetospheres is essential for analyzing (exo) planetary responses to varying stellar wind conditions. This differentiation is crucial for future space missions aimed at characterizing (exo)planetary magnetic environments and assessing atmospheric retention. Analyzing the diverse magnetospheric responses can help identify optimal observational strategies for detection of planetary magnetospheres.

The relative strength of planetary to stellar wind magnetic field plays a crucial role in determining the planetary dynamics and atmospheric mass loss (S. Gupta et al. 2023). Although temporary distortions and local reconnection events may occur in intrinsic magnetospheres—like that of Earth's—the global magnetic-field topology maintains its overall structure during ICME impacts (R. L. McPherron et al. 2008; Q. Zong 2022). However, as observed for Venus and Mars, imposed magnetospheres exhibit strong variations in response to the changes in stellar wind magnetic-field configurations (E. Dubinin et al. 2013a; Y. Futaana et al. 2017; S. Xu et al. 2020). These distinct responses have been observed through both in situ measurements (J. A. Slavin et al. 1991; J. Trotignon et al. 1993; C. Russell et al. 2006) and numerical simulations (S. Preusse et al. 2007; M. J. Way & A. D. Del Genio 2020; A. Basak & D. Nandy 2021). This reconfiguration of the magnetosphere can serve as a signature for characterizing (exo)planetary magnetic environments. The magnetotail lobes and current sheet dynamics also provide crucial insights into magnetospheric dynamics forced by stellar magnetism. Current density evolution in magnetotail regions is governed by the drift of charged particles along magnetic-field lines, with significant variations observed during different stellar wind and ICME interactions (G. A. DiBraccio et al. 2015; L. Wang et al. 2023).

Previous observational studies have demonstrated a diminished heavy-ion flux in the near-Venusian magnetotail during polarity reversal events, attributing these phenomena to magnetic detachment of plasma tails from the Venusian ionosphere (D. Vech et al. 2016). The magnitude of current density is intrinsically linked to the available charge carriers and the complex magnetic reconnection processes occurring during stellar wind (exo)planet interactions. Understanding these current density dynamics becomes crucial for comprehending energy transfer mechanisms, plasma interactions, and the overall response of (exo)planetary magnetospheres to varying stellar wind conditions. Atmospheric escape is another manifestation of star–planet interactions in (exo)planetary environments; e.g., it has been demonstrated that the efficiency of atmospheric loss is strongly influenced by the strength and orientations of stellar and planetary magnetic fields (S. Gupta et al. 2023).

Polarity reversals of the induced magnetosphere in response to changes in the ambient IMF direction are one of the most distinctive signatures of stellar magnetic forcing for unmagnetized bodies. At Venus and Mars, such reversals have been studied observationally and numerically (T. L. Zhang et al. 2008; E. Dubinin et al. 2013b; D. Vech et al. 2016; G. Li et al. 2023). In all of these studies, the driver is a heliospheric current sheet (HCS) or IMF sector-boundary crossing—i.e., a

quasi-steady rotation of the ambient IMF direction. D. Vech et al. (2016) provided the first statistical characterization of HCS-driven reversals and found a reduction of the near-tail heavy-ion flux and enhanced ion heating following the reversal event. The modeling efforts by Y.-D. Jia et al. (2007), M. Benna et al. (2009), and Y. D. Jia et al. (2009) further explored the polarity reversal process at Venus in response to changes in the ambient IMF direction. Building on this body of work, the present study examines the reversal process under transient, strongly magnetized CME-flux-rope driving and across a range of planetary magnetic-field strengths, thereby extending the analysis from the specific solar system unmagnetized case to a broader exoplanetary regimes.

Direct observations of (exo)planetary magnetic fields have not yet been achieved, although some techniques such as Lyα and radio emissions offer promise for indirect detection through star–planet magnetic interactions (P. Zarka 1998, 2007; J.-M. Grießmeier et al. 2007; G. Hallinan et al. 2008; I. F. Shaikhislamov et al. 2016; K. G. Kislyakova et al. 2019). Recently, wind-speed measurements in ultrahot Jupiters have provided indirect evidence of planetary magnetic fields of a few Gauss, via ohmic drag (J. V. Seidel et al. 2026). Radio emissions have been observed in several solar system planets, providing insights into their magnetic environments (A. Masters 2012; W. S. Kurth et al. 2016; L. Lamy et al. 2017; J. E. P. Connerney et al. 2018). Radio emissions arise from energy dissipation due to magnetic reconnection events during stellar wind and planetary magnetic-field interactions. Nevertheless, direct radio detections from (exo)planets remain elusive (T. S. Bastian et al. 2000; A. M. S. Smith et al. 2009; T. Murphy et al. 2015; C. R. Lynch et al. 2018; J. D. Turner et al. 2021). This creates a gap in our understanding of how planetary magnetic fields can be constrained through remote observations. In this context, magnetohydrodynamic (MHD) simulations provide a useful tool and guidance for exploring these complex star–planet interaction processes (S. B. Das et al. 2019; A. A. Vidotto & A. Cleary 2020; A. Basak & D. Nandy 2021; J. Varela et al. 2022a, 2022b; S. Gupta et al. 2023; S. Roy & D. Nandy 2023). In this study, we employ 3D MHD simulations to investigate the effects of different IMF and ICME orientations on (exo)planetary dynamics, atmospheric escape rates, and magnetotail current density structures for both magnetized and unmagnetized (exo) planets.

We limit our study to far-out, Earth-like planetary systems with varying magnetism, keeping in mind the perspective that such exoplanets are more likely to be habitable as opposed to close-in hot-Jupiter-like exoplanets; the latter systems, while more easily observed, are subject to more intense and complex stellar forcing, making them unlikely to be habitable (O. Cohen et al. 2014; A. A. Vidotto et al. 2015; J. J. Fortney et al. 2021).

Based on our qualitative analysis, we investigate whether the differential response of induced and intrinsic magnetospheres to CME driving can serve as a diagnostic for distinguishing between magnetized and unmagnetized (exo) planets. The subsequent sections of this paper are structured as follows: Section 2 provides a comprehensive description of the theoretical framework and numerical setup utilized in our study. Section 3 details our findings, followed by concluding remarks in Section 4.

2. Model Description

We adapt the 3D MHD STORM Interaction Module (CESSI-STORMI) developed by S. Roy & D. Nandy (2023) to simulate the impact of different orientations of stellar wind and ICMEs on (exo)planetary magnetospheres with different intrinsic magnetic-field strengths. The STORMI model includes the capability to model magnetized CME flux ropes and is implemented as an enhancement of the star–planet interaction module previously developed by S. B. Das et al. (2019) based on the PLUTO MHD solver (A. Mignone et al. 2007). In this model, the interactions are governed by the adiabatic equation of state and the following set of resistive MHD equations:

$$\partial_t \rho + \nabla \cdot (\rho \boldsymbol{v}) = 0 \tag{1}$$

$$\partial_t \boldsymbol{v} + (\boldsymbol{v} \cdot \nabla)\boldsymbol{v} + \frac{1}{4\pi\rho}\boldsymbol{B} \times (\nabla \times \boldsymbol{B}) + \frac{1}{\rho}\nabla P = \boldsymbol{g} \tag{2}$$

$$\partial_t E + \nabla \cdot [(E + P)\boldsymbol{v} - \boldsymbol{B}(\boldsymbol{v} \cdot \boldsymbol{B}) + (\eta \cdot \boldsymbol{J}) \times \boldsymbol{B}] = \rho \boldsymbol{v} \cdot \boldsymbol{g} \tag{3}$$

$$\partial_t \boldsymbol{B} + \nabla \times (\boldsymbol{B} \times \boldsymbol{v}) + \nabla \times (\eta \cdot \boldsymbol{J}) = 0. \tag{4}$$

The symbols ρ, $\boldsymbol{v}$, $\boldsymbol{B}$, $\boldsymbol{J}$, P, E, and $\boldsymbol{g}$ denote density, velocity, magnetic field, current density, pressure, total energy density, and gravitational acceleration due to the planet, respectively. We consider a finite and isotropic magnetic diffusivity η, as the causal mechanism for nonideal processes such as magnetic reconnections. The magnetic diffusivity lies within the range of realistic values as shown in earlier studies (J. Raeder 1999; C. M. Komar et al. 2013; J. Varela et al. 2022a). While anisotropic diffusivity may capture fine scale dynamics near current sheets more accurately, we use this simplified treatment, as our focus is on the qualitative, global-scale dynamics. The expression for total energy density is given by

$$E = \frac{P}{\gamma - 1} + \frac{\rho v^2}{2} + \frac{B^2}{8\pi} \tag{5}$$

for an ideal gas equation of state.

The computational domain extends from $[-145, 205\ ]R_p$ in the x-direction, $[-100, 100]R_p$ in the y-direction and $[-145, 145]R_p$ in the z-direction, where R_p is the planetary radius, with the planet located at the origin (0,0,0) of the Cartesian box. We use a nonuniform grid to ensure computational efficiency while attaining the desired resolution in specific regions of interest. The region extending from -5 R_p to 5 R_p is resolved by 40 grid cells in all three directions. In the x-direction, for the outermost regions extending from -145 R_p to -100 R_p, and from 100 R_p to 205 R_p, one grid cell corresponds to 3 R_p. Moving inward, in the regions between -100 R_p to -50 R_p and between 50 R_p to 100 R_p, one grid cell corresponds to 2 R_p. In the regions extending from -50 R_p to -25 R_p and 25 R_p to 50 R_p, one grid cell represents R_p. Closer to the planet from -25 R_p to -10 R_p and from 10 R_p to 25 R_p, two grid cells represent R_p. Further refinement occurs between -10 R_p to -5 R_p and 5 R_p to 10 R_p, where three grid cells represent R_p. The same progressive grid refinement is applied in both the y- and z-directions, ensuring greater resolution near the planetary vicinity and coarser resolution farther away. We have also performed some relatively higher-resolution runs to test the sensitivity of our results to grid size; these are reported in Appendix A. The grid resolution employed in this study

(0.25 R_p baseline, 0.1 R_p in Appendix A) is appropriate for investigating large-scale magnetospheric topology and global dynamics rather than local, kinetic-scale reconnection physics (B. B. Tang et al. 2009; C. Wang et al. 2014; S. Turnpenney et al. 2020; J. Varela et al. 2022a). Our scientific objectives—studying global polarity reversals, relative atmospheric escape rates across different configurations, and magnetotail current evolution—can be well characterized with the resolution employed in this study.

To study the effect of stellar magnetic-field orientation on planetary atmospheric loss, we approximate the atmosphere as a conducting plasma surrounding the planet. While this approximation may overestimate the atmospheric mass-loss rate, our primary objective, herein, has been to investigate the qualitative magnetospheric response to different stellar magnetic-field configurations. Similar large-scale MHD treatments of planetary plasma environments have been employed in studies of star–planet interactions and atmospheric escape (Y. J. Ma et al. 2013; O. Cohen et al. 2015; S. B. Das et al. 2019; A. Basak & D. Nandy 2021; S. Gupta et al. 2023; S. Roy & D. Nandy 2023). The density profile in the vicinity of the planet is defined by

$$\begin{aligned} \rho_{\rm pl} &= 10^6 \rho_{\rm amb} \qquad r \leqslant R_p, \\ \rho_{\rm atm}(r) &= \rho_{\rm pl} + \frac{(\rho_{\rm amb} - \rho_{\rm pl})}{2}\left[\tanh\left\{9\left(\frac{r}{R_P} - 2\right)\right\} + 1\right] \\ & R_P \leqslant r \leqslant 3R_p, \end{aligned} \tag{6}$$

where $\rho_{\rm pl}$, $\rho_{\rm amb}$, and r represent the densities of the planet and the ambient medium and radial distance from the origin, respectively. For details on the choice of this atmospheric profile, refer to A. Basak & D. Nandy (2021). The atmospheric distribution of pressure is calculated assuming a hydrostatic equilibrium condition:

$$\frac{dP}{dr} = -\rho_{\rm atm}(r) g(r). \tag{7}$$

Here, acceleration due to gravity is given by $g(r) = -\frac{GM_{\rm pl}}{r^2}$, where $M_{\rm pl}$ is the planetary mass. The pressure inside the planet's core is kept constant and is equal to its value on the planetary surface.

Table 1 summarizes the physical values and notation used in our simulations. The ambient density, pressure, and nominal solar-wind speed are chosen to be representative of near-Earth solar-wind conditions. However, the qualitative implications are applicable to other far-out star–planet systems, and can be quantitatively scaled for more extreme stellar wind and CME properties observed in young, active, or cool stars (O. Cohen et al. 2014; A. A. Vidotto et al. 2015; B. E. Wood et al. 2021). For a parameter-space study using a range of stellar and planetary magnetic-field strengths, see S. Gupta et al. (2023). The density and pressure in the region $r > 3R_{\rm pl}$ is initialized to be equal to that in the ambient medium.

In the model setup, the planetary dipolar magnetic field is first forced from the left boundary of the computational box with the nominal stellar wind for up to 240 minutes, allowing the stellar wind to establish a wind-forced quasi-steady magnetospheric configuration before the ICME is introduced. A common time is adopted for all simulations to ensure identical initial conditions prior to CME injection (S. B. Das et al. 2019; A. Basak & D. Nandy 2021; S. Gupta et al. 2023).

Table 1
Values of Physical Parameters Used in the Simulations and Their Respective Notations

Physical Quantity	Notation	Value Used
Density in ambient medium	$\rho_{\rm amb}$	1.5×10^{-23} g cm^{-3}
Pressure in ambient medium	$P_{\rm amb}$	2.49×10^{-11} dyne cm^{-2}
Density of stellar wind in nominal conditions	$\rho_{\rm sw(N)}$	4 $\rho_{\rm amb}$
Density of stellar wind during ICME	$\rho_{\rm sw(ICME)}$	12.89 $\rho_{\rm amb}$
Velocity of stellar wind in nominal conditions	$v_{\rm sw(N)}$	4×10^7 cm s^{-1}
Velocity of stellar wind during ICME	$v_{\rm sw(ICME)}$	10×10^7 cm s^{-1}
Adiabatic index	γ	5/3
Planetary mass	$M_{\rm pl}$	5.97×10^{27} g
Planetary radius	$R_{\rm pl}$	6.37×10^8 cm
Intrinsic planetary magnetic field	$B_{\rm pl}$	0–2B_e[a]
Stellar wind magnetic-field magnitude in nominal conditions	$B_{\rm sw(N)}$	10 nT
Stellar wind magnetic-field magnitude at the center of CME flux rope	$B_{\rm 0cme}$	38 nT
Magnetic diffusivity	η	10^{13} cm^2 s^{-1}
Magnetospheric tilt angle	$\theta_{\rm pl}$	11°

Note.
[a] The symbol B_e represents the magnetic field for the case of the Earth's dipole.

After the IMF, an ICME shock and sheath followed by an idealized ICME flux rope are injected into the computational domain. We model the flux ropes using the force-free nonlinear flux-rope model developed by Gold and Hoyle (T. Gold & F. Hoyle 1960; Q. Hu et al. 2014). Following the ICME transit, we again introduce the IMF forcing on the planetary magnetosphere to simulate the relaxation of the magnetospheric system in the aftermath of the storm. In our modeled Gold–Hoyle flux rope, the twist is radially uniform, and the helicity is positive. The magnetic-field components in curvilinear cylindrical coordinates ($x = r\cos\phi$, $x = r\sin\phi$, $z = z$) are:

$$B_r = 0$$

$$B_\phi = \frac{Tr}{1 + T^2 r^2} B_0$$

$$B_z = \frac{1}{1 + T^2 r^2} B_0.$$

Here, B_0 is the magnitude of the magnetic field at the axis of the flux rope, and T is a constant representing the twist per unit length in the form of $\tau = T/2\pi$. The corresponding values adopted in this study are listed in Table 1.

In this study, we focus on a far-out Earth-like planet with an Earth-like mass, radius, and dipolar tilt, while the nominal stellar wind is assumed to have a speed of 350 km s^{-1}, corresponding to quiet times observed in the Sun–Earth system. The ICME is assumed to have a speed of 1000 km s^{-1}. We perform a set of simulations, as illustrated in Figure 1, by varying the orientation of the IMF and the embedded ICME magnetic field. Specifically, we consider four cases: northward IMF followed by northward ICME in time (nIMF-nICME), northward IMF followed by southward ICME (nIMF-sICME), southward IMF followed by northward ICME (sIMF-nICME), and southward IMF followed by

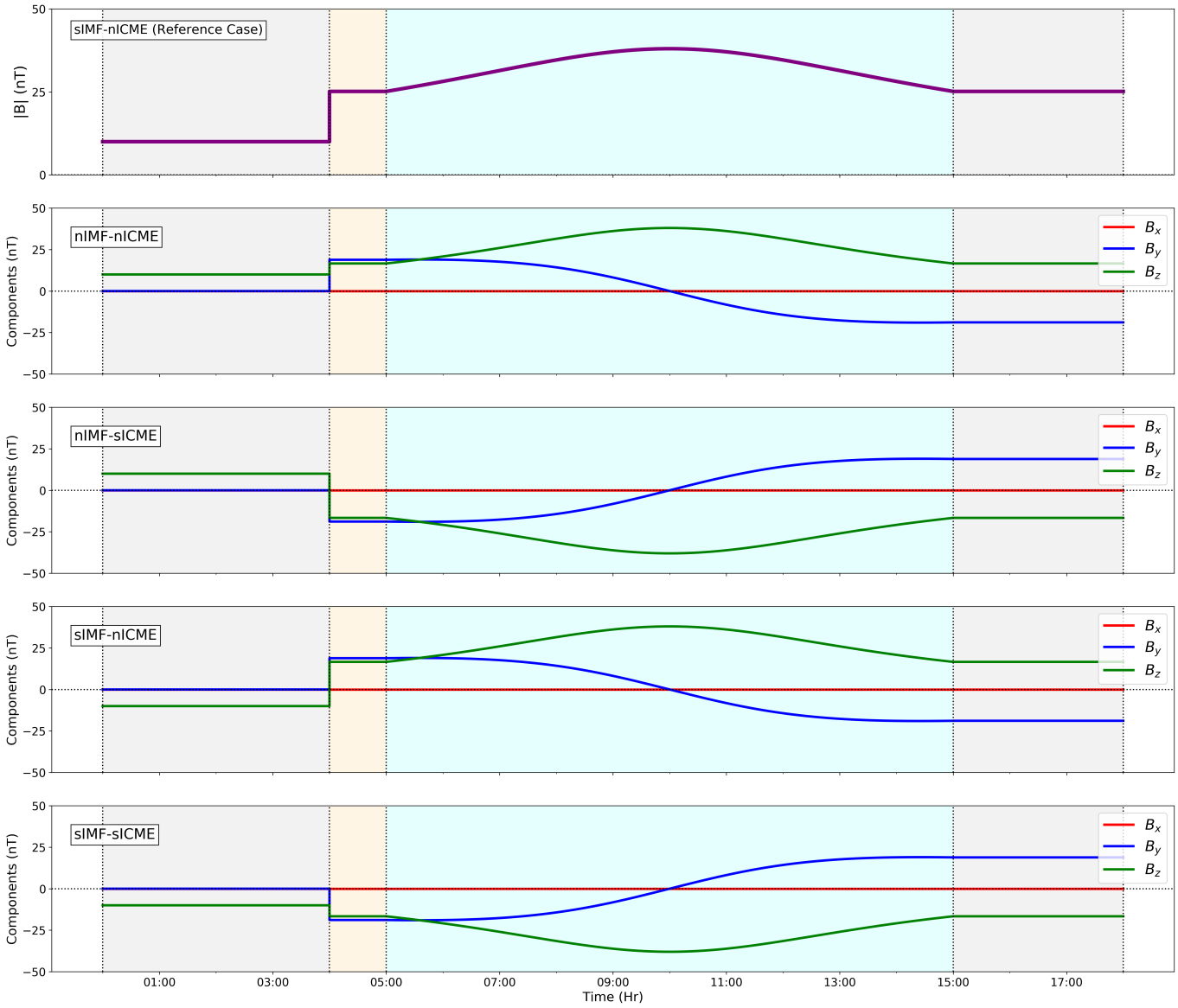


Figure 1. Temporal evolution of the stellar magnetic-field conditions used as boundary inputs in the simulations. The top panel shows the total field magnitude ($|B|$), and the lower panels depict the Cartesian components (B_x, B_y, B_z) for each IMF-ICME orientation case. Shaded regions indicate the pure IMF (gray), ICME sheath (beige), and ICME flux-rope (blue) phases followed by pure IMF.

southward ICME (sIMF-sICME). The terms "northward ICME" (nICME) and "southward ICME" (sICME) refer to the orientation of the axial magnetic field of the flux-rope ejecta, such that "northward" corresponds to positive B_z and "southward" to negative B_z. This is the standard convention adopted in near-Earth ICME magnetic-configuration studies (V. Bothmer & R. Schwenn 1998; T. Mulligan et al. 1998; E. Palmerio et al. 2018; S. Pal et al. 2022).

For each configuration, we also vary the strength of the planetary magnetosphere from unmagnetized to $0.1B_e$, B_e, and $2B_e$ and perform simulations with all possible combinations. Here, $B_e = 3.1 \times 10^4$ nT denotes the surface equatorial magnetic-field strength of the Earth's dipolar field.

Figure 1 presents the temporal evolution of the upstream magnetic-field conditions that we consider as boundary inputs in our simulations. The top panel shows the total magnetic-field magnitude ($|B|$), while the next four panels display the three Cartesian components (B_x, B_y, B_z) for each IMF-ICME orientation case. The shaded regions distinguish the different phases: the initial steady IMF, the ICME sheath, and the ICME flux rope, followed by a return to the background IMF. In each case, the simulation begins with a constant IMF, after which the ICME sheath arrives, resulting in a step-like increase in $|B|$ as expected at the shock front. The subsequent flux-rope phase exhibits a smoothly varying rotation of the field components, representing the passage of the ICME structure. Although the four cases differ in the orientation and temporal evolution of the magnetic-field components, we ensure that the total magnetic-field magnitude remains the same across all cases, as depicted in the top panel. Our simulation setup enables identification of how field orientation influences planetary magnetospheric responses by maintaining a consistent magnetic pressure across all IMF-ICME cases.

The input parameters at the stellar wind injection boundary (at $x = -145\ R_p$ in the yz-plane) are obtained by solving the Rankine–Hugoniot conditions for the given shock velocity.

The density and pressure during the ICMEs are also defined by solving the Rankine–Hugoniot conditions to generate and maintain the shock fronts. For all other boundary faces of the Cartesian box, an outflow boundary condition is implemented. We consider a peak magnetic-field strength of 38 nT for the ICME flux-rope ejecta, representative of a strong magnetized CME in the inner heliosphere (S. Good & R. Forsyth 2016; M. Janvier et al. 2019). The objective of the present study is not to reproduce a specific observed CME event, but rather to investigate the qualitative magnetospheric response to a strongly magnetized stellar disturbance across planets with different intrinsic magnetic-field strengths. The magnetic-field orientation of the stellar wind and (or) planetary magnetic-field strength are varied in each computational run; additionally, the steady-state configuration of the planetary magnetosphere, atmospheric loss, global magnetic polarity, and magnetotail current density are analyzed.

3. Results and Discussion

The interaction of stellar CMEs and planetary magnetic configurations results in a complex, dynamically evolving system shaping the space environment around the (exo) planetary magnetosphere. Our 3D MHD simulations provide insights into the governing dynamics, and we explore interactions across varying (exo)planetary magnetic-field strengths and ICME magnetic-field orientations. In subsequent sections, we discuss our analysis focusing on global planetary magnetospheric configurations, magnetic polarity reversal, magnetotail current density evolution, and atmospheric mass-loss rates.

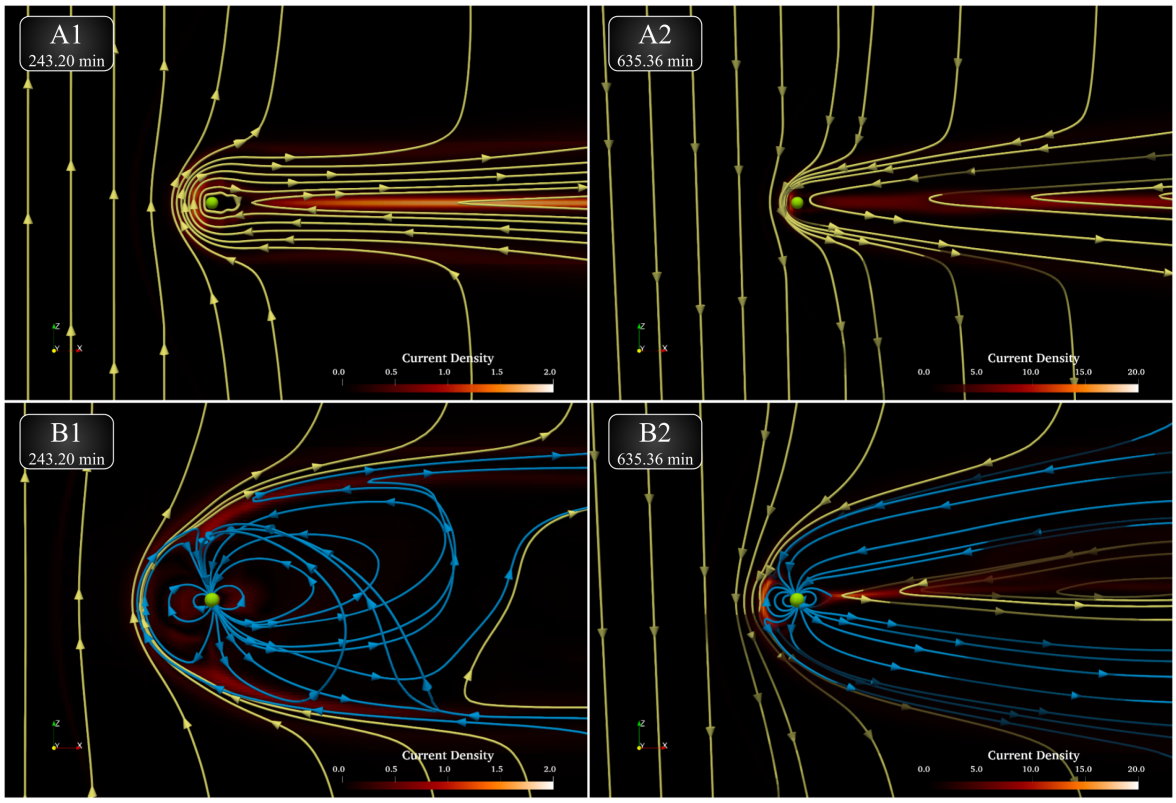
3.1. Global Magnetic Polarity Reversal Dynamics

Stellar wind and CMEs play a crucial role in shaping the planetary magnetosphere, with the orientation of the stellar wind magnetic field exerting a significant influence on the configuration of magnetospheric structures. D. Vech et al. (2016) discussed the statistical features of global polarity reversal of the Venusian induced magnetosphere in response to changes in the orientation of the IMF due to HCS crossings. Here, we investigate the impact of the transient, magnetized CME-flux rope and, in addition, examine how the polarity reversal response depends on the intrinsic planetary magnetic-field strength. We perform 3D MHD simulations to explore the effects of stellar wind and ICME magnetic-field orientation on (exo)planetary magnetospheres with different magnetic-field strengths. Figure 2(a) illustrates the global magnetic configuration for the unmagnetized and magnetized planet ($B_p = 2\ B_e$) when impacted by the stellar wind conditions shown in panel 3 of Figure 1. The left panels ((A) and (C)) of Figure 2(a) show the steady-state configuration when the planetary magnetosphere interacts with only nominal northward-oriented stellar wind, and the right panels ((B) and (D)) represent the state when planetary magnetosphere interacts with southward-oriented ICME. In these plots, yellow and blue lines represent the streamlines of the stellar wind and the planetary magnetic field, respectively. Vectors indicate the direction of the magnetic field, and the current density is plotted as the background in each figure.

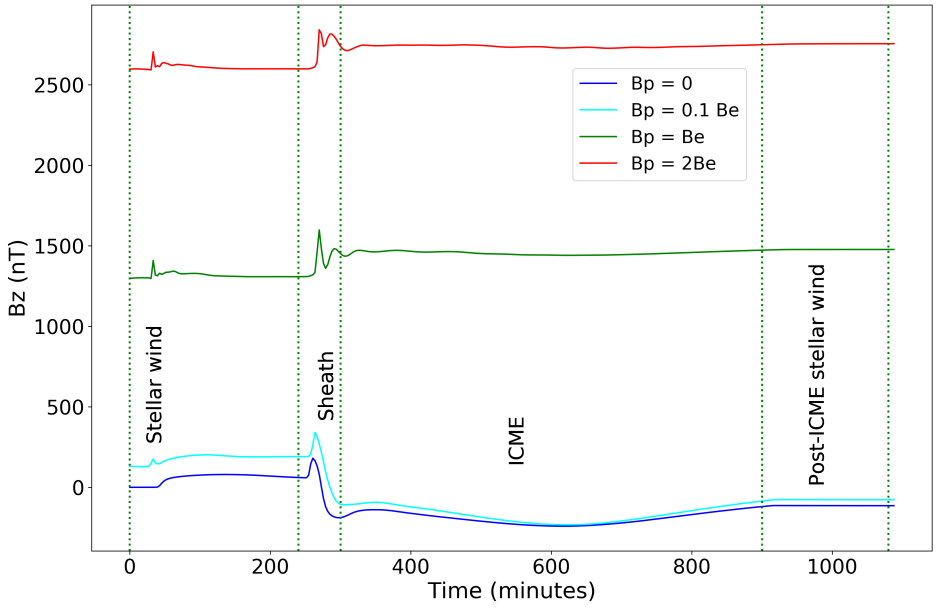
The top panel of Figure 2(a) ((A) and (B)) demonstrates the global polarity reversal for the induced magnetosphere of the unmagnetized planet, which has been conditioned by a northward-oriented stellar wind (thereby picking up a clockwise magnetic field when viewed from the positive to negative y-direction), followed by a southward-oriented ICME (note the magnetic field becomes counterclockwise when viewed from the same perspective). As the ICME with oppositely directed magnetic-field orientation relative to the nominal stellar wind magnetic field interacts with the planet, magnetic reconnection occurs for a brief duration. Subsequently, the imposed magnetosphere reconfigures and reverses, aligning with the external stellar CME magnetic-field orientation. Our analysis indicates that the planetary magnetic-field strength influences the susceptibility to stellar wind-induced polarity reversals. For weakly magnetized planets ($B_p = 0.1\ B_e$), the stellar wind or a CME magnetic field can still induce polarity reversals (Figure 2(b)). However, as the planetary magnetic field increases ($B_p = B_e$ or $B_p = 2\ B_e$), the magnetosphere becomes increasingly resistant to reversals, even when forced by a CME. It maintains its intrinsic polarity in the vicinity of the planet, when exposed to an oppositely directed ICME (Figure 2(b)). The results suggest that the relative strengths of planetary and stellar wind magnetic fields are fundamental to determining the potential for global polarity reversals in (exo)planetary magnetospheres. A similar reconfiguration of the imposed magnetosphere takes place during the sIMF-nICME event. For nIMF-nICME and sIMF-sICME events, the imposed magnetosphere maintains the same configuration dictated by the unchanging external stellar wind magnetic-field orientation. This behavior is expected and may be considered as the "control" experiment. A strongly magnetized planet maintains its intrinsic polarity for all cases of IMF-ICME events.

Our simulations demonstrate that the response of a planetary magnetosphere to stellar CME-induced polarity reversal is strongly modulated by the planet's intrinsic magnetic-field strength. In the absence of an intrinsic magnetic field, the planetary ionosphere interacts directly with the stellar wind, leading to the formation of an induced magnetosphere. The polarity of this induced magnetosphere is dictated by the orientation of the stellar wind magnetic field. When the stellar wind magnetic field reverses its orientation, the induced magnetosphere rapidly reconfigures, resulting in a global polarity reversal. In contrast, planets with strong intrinsic magnetic fields are less susceptible to polarity reversal. The intrinsic field dominates the interaction, shielding the planet from the direct influence of the stellar wind. While the magnetosphere may compress or undergo local reconnection events, the overall magnetic topology remains stable.

To further illustrate the polarity reversal, we plot the Z-component of the magnetic field at the planetary day side at a distance of 2.8 R_p (Figure 2(b)). The magnetic field is evaluated at a distance of 2.8 R_p on the planetary dayside. This location is chosen such that it remains inside the planetary magnetosphere (or induced magnetosphere for the unmagnetized case) across all of the simulations, including during periods of maximum CME-induced compression. Consequently, the measured magnetic field at a chosen location reflects the planetary magnetospheric configuration rather than the upstream stellar or ICME magnetic field. Figure 2(b) shows that at the distance of 2.8 R_p, the magnetic field reverses



(a)



(b)

Figure 2. Polarity reversal in (exo)planetary magnetospheres. (a) Evolution of magnetic-field streamlines, with blue representing (exo)planetary magnetic field and yellow representing stellar wind magnetic-field lines during planetary interaction with the stellar wind. (A1) is the steady-state configuration when northward stellar wind interacts with the unmagnetized planet (t = 243.2 minutes). (A2) shows the magnetospheric configuration of unmagnetized planet during the southward-oriented ICME interaction with the planet (t = 635.36 minutes). The plots show the global polarity reversal when transitioning from northward nominal stellar wind to southward ICME. (B1) and (B2) show similar interaction for a magnetized planet ($B_p = 2B_e$), showing that polarity does not reverse in the vicinity of the planet. (b) Z-component of the magnetic field at 2.8 R_p on the planetary dayside, illustrating that the polarity reversal at the vicinity of the planet diminishes with increasing (exo)planetary magnetic-field strength.

its direction for unmagnetized and weakly magnetized planets ($B_p = 0$ and $B_p = 0.1\ B_e$), as depicted by the blue and cyan curves, respectively. However, as the planetary magnetic-field strength increases (for cases, $B_p = B_e$, and $2B_e$), the intrinsic planetary magnetic field (green and red curves) do not flip their direction; i.e., the planet retains its native magnetic-field orientation.

The transition to polarity-reversing behavior does not appear to occur at a single threshold magnetic-field strength but rather over a range of intrinsic planetary magnetic-field strengths determined by the relative strength of the external stellar magnetic forcing and the intrinsic planetary dipole field. To investigate this transition further, we perform additional simulations for intermediate planetary magnetic-field strengths of $B_p = 0.3\ B_e$ and $B_p = 0.5\ B_e$ under identical stellar wind and ICME conditions. As shown in Figure B1 of Appendix B ("Additional Simulations of the Polarity Reversal Transition"), these simulations indicate that increasing planetary magnetic-field strength progressively suppresses the polarity reversal response. For $B_p = 0.3\ B_e$, the CME interaction produces a substantial reduction in the near-planet magnetic-field strength and significant magnetospheric reconfiguration, although a sustained global polarity reversal is not attained. For $B_p = 0.5\ B_e$, the intrinsic dipolar topology remains largely intact during the external stellar wind magnetic-field reversal. These results suggest that the transition from induced to intrinsic magnetospheric behavior is governed by the competing influences of the stellar forcing's magnetic properties and the intrinsic planetary magnetic-field strength.

3.2. Magnetotail Current Density Dynamics

The external stellar wind conditions significantly influence the current density dynamics in the planetary magnetosphere. D. Vech et al. (2016) presented observational evidence of diminished heavy-ion flux in the near-Venus magnetotail during polarity reversal events—attributing this phenomenon to the magnetic detachment of the plasma tail from the planetary ionosphere. The drift of charged particles along magnetic-field lines governs current density in the magnetotail. A reduction in ion flux impacts the available charge carriers for current flow, leading to a drop in current density. Our MHD simulation approach cannot capture microscale physics; however, qualitatively, our results corroborate the observational findings of D. Vech et al. (2016). Our analysis indicates a decrease in current density magnitude near the magnetotail of an unmagnetized planet during polarity reversal events analogous to observations for Venus.

We compute the current density magnitude on the planetary night side (spanning from 1.5–5 R_p along the x-axis). To account for current sheet thickness, we average the current density across the yz-plane, ranging from –1 to 1 R_p in both y- and z-directions. Figure 3 illustrates the evolution of current density magnitude during ICME interactions for planets with varying magnetic-field strengths. Each panel in Figures 3(a)–(d) represents a different planetary magnetic-field strength, and within each panel, the current density magnitude is plotted as a function of distance along the x-axis (planetary night side) at different times during the simulation. The black curve in each panel represents the steady-state current density profile during the initial interaction of the planet with nominal stellar wind. Other curves show the current density profiles at indicated time instances during the ICME impact and passage. The first row in each panel illustrates cases where a northward IMF is followed by northward and southward ICMEs, while the second row depicts cases where a southward IMF is followed by northward and southward ICMEs, respectively. For the unmagnetized planet, Figure 3(a), we find that the current density is consistently lower in magnitude when an oppositely directed ICME (relative to the previous nominal stellar wind IMF) interacts with the planet. The column-wise plot of Figure 3(a) indicates that initially, the current density magnitude is lower for the cases where polarity reversal occurs (columns 1 and 2 of Figure 3(a)). However, following some time, the current density slowly recovers, regardless of stellar wind magnetic-field orientation (columns 3 and 4 of Figure 3(a)).

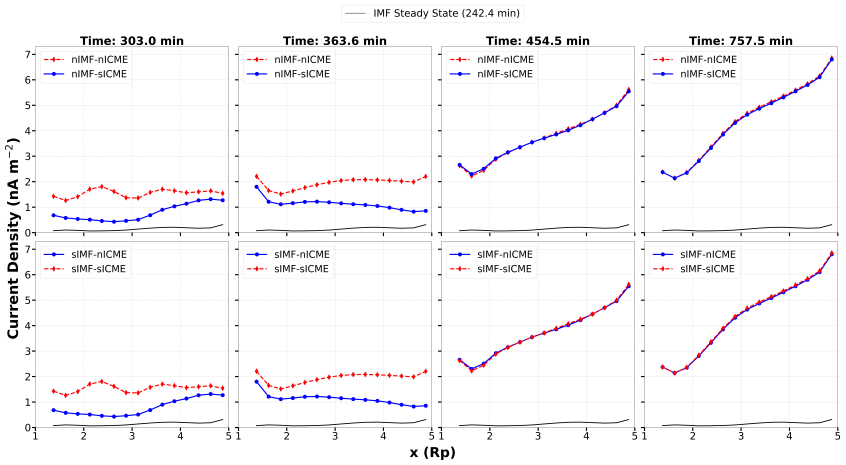
We analyze current density dynamics in the vicinity of the planet, extending up to 5 R_e on the nightside, where the influence of the intrinsic planetary magnetic field dominates. Within this spatial window, the steady-state current density profiles for northward and southward IMF orientations appear similar. However, at larger distances in the magnetotail, such as at 10 R_e and beyond, the differences between the nIMF and sIMF cases become more pronounced. As we move far away from the planet, the distinct polarity reversal central to our analysis is less discernible. Thus, we confine our analysis to within 5 R_e on the magnetotail side.

When IMF or ICME is oriented antiparallel to the planet's intrinsic magnetic field at the dayside magnetopause, magnetic reconnection occurs. The reconnected field lines are then swept away from the stellar side toward the planetary magnetotail, where further reconnection follows. This process drives a continuous cycle of magnetic flux transfer—known as the Dungey cycle—which enhances plasma convection and increases current densities in the magnetotail region (R. C. Fear et al. 2019; S. E. Milan et al. 2021; A. Paul et al. 2023). For magnetized planets (Figures 3(b)–(d)) $B_p = 0.1\ B_e$, B_e, and $2\ B_e$, current density magnitude is elevated when a southward-oriented ICME interacts with the planetary magnetosphere. The elevation can be attributed to enhanced magnetic reconnection between the southward IMF and the northward-oriented planetary magnetic field. This enhancement in current density can be fundamentally explained by the Dungey cycle, which describes the large-scale circulation of magnetic flux and plasma within a planetary magnetosphere due to solar-wind-magnetosphere coupling.

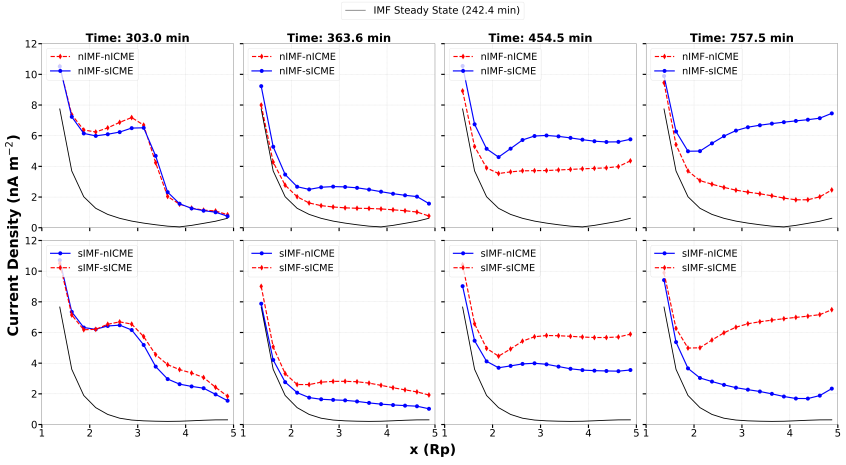
Our analysis suggests that these distinct magnetotail current density responses can serve as indicators of a planet's magnetic environment, distinguishing between intrinsic and induced magnetospheres in future observational studies.

3.3. Atmospheric Escape Rate

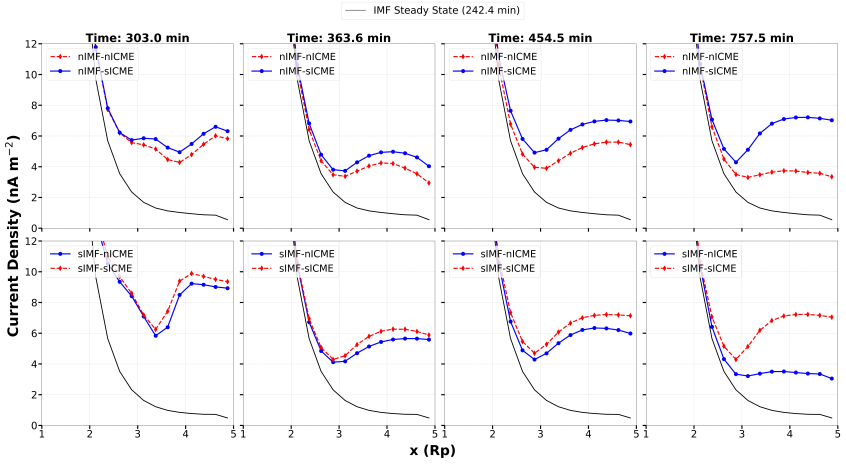
Of the many mechanisms responsible for atmospheric escape, stellar winds and CMEs are major factors that can contribute to atmospheric mass loss. Other important processes include high-energy radiation (XUV), ion pickup, and solar energetic particles (SEPs). However, we limit our study to atmospheric losses driven by magnetized CMEs and stellar winds, rather than those caused by high-energy radiation, ion pickup, or SEPs. The latter mechanisms can play a dominant role in specific evolutionary phases of planets or host stars or in close-in exoplanetary systems (R. D. Jolitz et al. 2023; G. Hazra et al. 2024b).



(a) Bp = 0

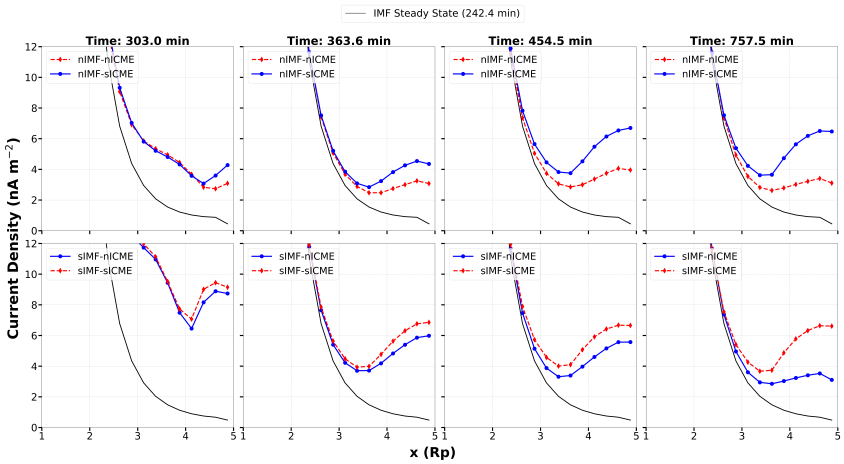


(b) Bp = 0.1Be



(c) Bp = Be

Figure 3. Current density magnitude evolution in the (exo)planetary magnetotail during ICME interaction. The panels show different (exo)planetary magnetic-field strengths: (a) $B_p = 0$ (unmagnetized), (b) $B_p = 0.1B_e$, (c) $B_p = B_e$, and (d) $B_p = 2B_e$. For each case, the temporal evolution is shown for various ICME magnetic-field orientations. The black curve represents steady-state nominal stellar wind interaction, while other curves show different time instances during ICME interaction. The blue curve indicates the scenario where the interplanetary magnetic field (IMF) followed by the ICME field is oppositely directed, whereas the red curve represents the case where the planet is impacted by an IMF followed by the same ICME magnetic-field orientation.



(d) Bp = 2Be

Figure 3. (Continued.)

Stellar wind and CMEs are the predominant factor resulting in the atmospheric escape of planets. The rate of atmospheric mass loss depends on the extent to which stellar wind penetrates into the planetary atmosphere. The extent of this stellar wind penetration is largely dependent on magnetic reconnections of the stellar wind magnetic field with the planetary magnetosphere and the dynamic ram pressure. The magnetic-field orientations of the IMF and ICMEs significantly influence the magnetic reconnection dynamics with the planetary magnetosphere and are, therefore, expected to influence the atmospheric escape rate.

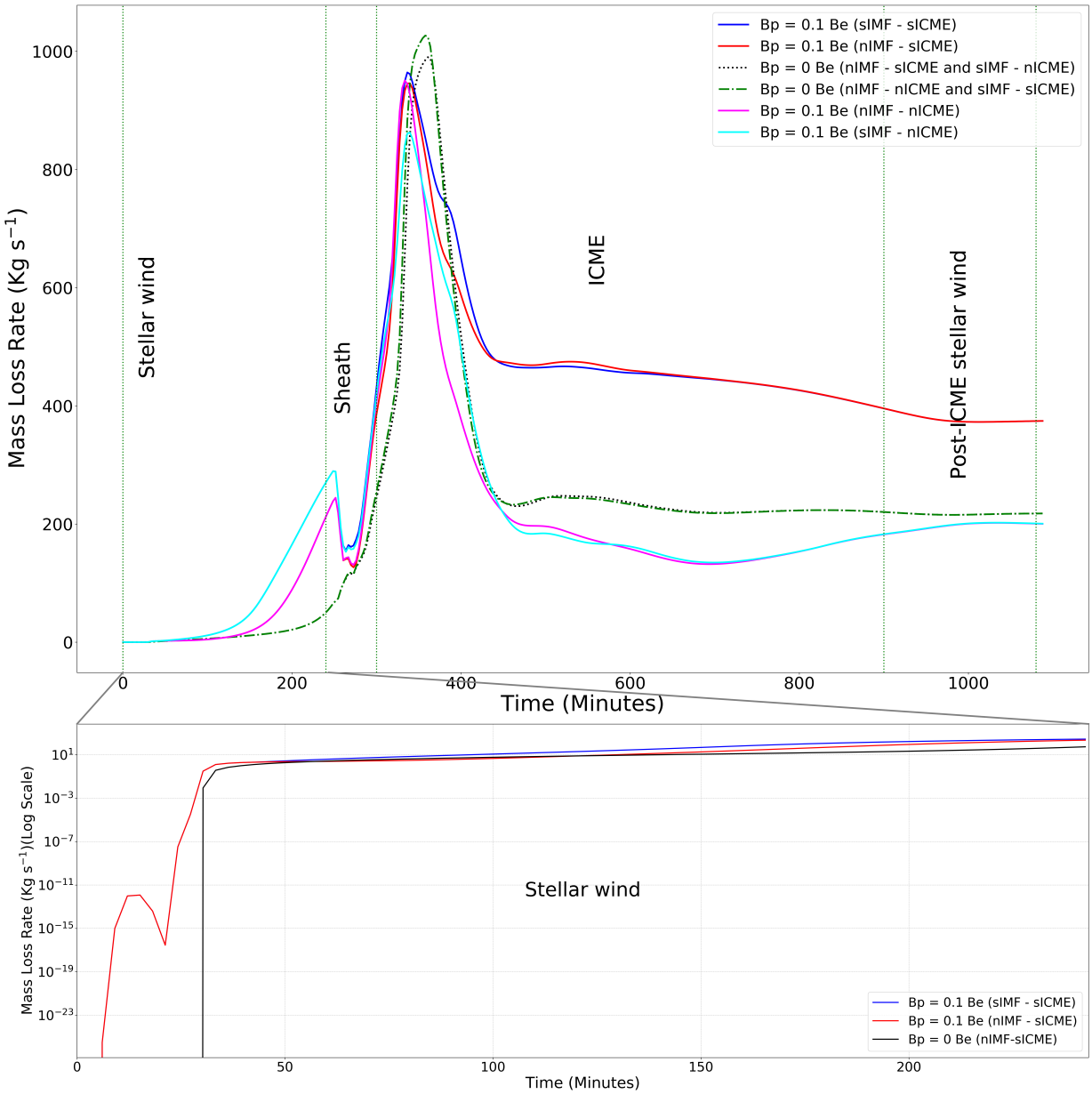
We perform a comparative analysis of atmospheric escape rates resulting from the interactions of different stellar wind and CME magnetic-field orientations relative to the planetary magnetosphere. To compute the total mass-loss rate, we consider a cube of edge length 10 R_p (extending from –5 R_p to 5 R_p in all three directions) with its geometric center coinciding with the center of the planet such that the whole planet—including its modeled atmosphere—is enclosed within the cube. Mass-loss rates are computed across all six faces of the cube, and loss rates from all six faces are summed up to obtain the total mass-loss rate.

Figure 4(A) illustrates the temporal evolution of atmospheric mass-loss rates for unmagnetized and weakly magnetized ($B_p = 0.1B_e$) planets during ICME interaction. Different plots show that for all cases of our simulations, the mass-loss rate initially experiences a brief dip as the ICME impacts the planet. This dip occurs due to the compression and confinement of the magnetosphere and modeled atmosphere caused by the impact of the ICME shock. However, following this initial compression, the mass-loss rate rises sharply as a result of large-scale compression of the magnetosphere and reconfiguration of the near-planet magnetic topology in response to the CME driving, which opens up regions of the magnetotail and cusp to enhanced plasma outflow. Eventually, the mass-loss rate reduces and stabilizes slowly in the recovery phase from the ICME impact. The steady state is less apparent in the linear plot (top panel of Figure 4(A)) due to the scale sensitivity to small changes. To address this, we include a log-scale plot of the initial stellar wind forcing in the bottom panel of Figure 4(A). The plot confirms that the system achieves a dynamical steady state forced by the wind, before the onset of ICME associated dynamics starting from approximately 240 minutes. We, therefore, focus on the subsequent phase to investigate the CME-associated dynamics and planetary response.

For all four combinations of IMF and ICME magnetic-field orientations for unmagnetized planets, the atmospheric mass-loss rates are similar. In contrast, for a magnetized planet ($B_p = 0.1\ B_e$), the mass-loss rates are significantly influenced by the orientation of the stellar magnetic field. Southward ICMEs induce much higher mass-loss rates compared to northward ICMEs in the case of magnetized planets (with a negative, Earth-like dipole field). For cases when the orientation of the stellar wind magnetic field aligns with the planetary magnetic field (i.e., both are northward oriented), the presence of a planetary magnetic field can provide shielding against atmospheric mass loss compared to the unmagnetized planet.

Unlike the case of a magnetized planet, in unmagnetized planets, reconnection dynamics does not play a major role in induced magnetospheres, and thus, the escape rate is nearly similar for different orientations of the magnetic field in unmagnetized planets. In Figure 4, we show a comparison of atmospheric mass-loss rates for $B_p = 0.1\ B_e$ and an unmagnetized planet. We consider only these cases, because, as we increase the planetary magnetic field, the box size to compute the atmospheric mass-loss rate also needs to be larger. Otherwise, the magnetopause boundary crosses the boundary of the box during the temporal evolution, resulting in spurious results. We have verified that for the other two cases as well (i.e., $B_p = B_e$ and $2B_e$), our results are qualitatively similar to those for $B_p = 0.1B_e$ but with a larger box size. For the plasma atmosphere, as considered in the present study, the mass-loss rate is higher for the planet with a stronger planetary magnetic field.

Figure 4(B) depicts the analysis of mass-loss rates across different planes around the planet. The plot indicates that the nightside region contributes predominantly to the atmospheric escape, with significant contributions from the cusp regions as well. This shows that the presence of an intrinsic magnetic field does not always shield the planet against atmospheric escape. Even for the Earth-like dipolar magnetic topology adapted in this work, the atmospheric mass loss



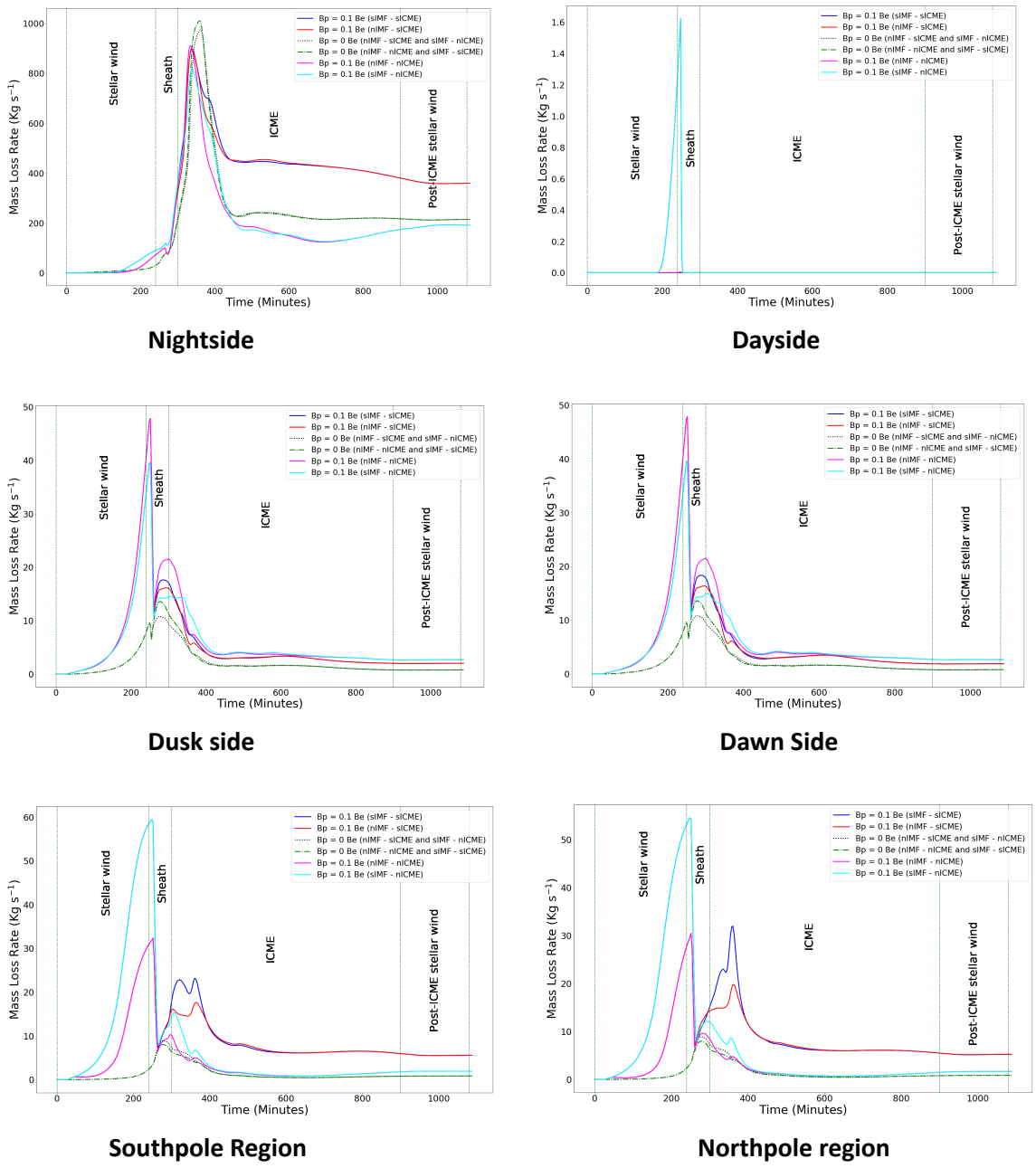
(A) Total Massloss rate

Figure 4. (A) Temporal evolution of atmospheric mass-loss rates for unmagnetized and magnetized ($B_p = 0.1B_e$) (exo)planets during stellar field interaction. Mass-loss rates are computed within a cubic volume ($\pm 5\ R_p$ in all directions) encompassing the planet and its atmosphere. Top panel: different curves represent various IMF-ICME orientation combinations, with vertical dashed lines marking key transition points: stellar wind, sheath region, ICME impact, and post-ICME stellar wind conditions. Bottom panel: the log-scale representation of the initial stellar wind forcing shows that the system has reached dynamical steady state well before the ICME forcing. (B) Analysis of atmospheric mass-loss rates through all six planes (nightside, dayside, dusk, dawn, south pole, and north pole).

depends strongly on the relative orientation between the external stellar magnetic field and the intrinsic planetary dipole. Configurations in which the stellar and planetary magnetic fields are oppositely oriented favor enhanced magnetic reconnection, leading to increased atmospheric escape through the cusp and magnetotail regions (H. Gunell et al. 2018; S. B. Das et al. 2019; H. Egan et al. 2019; S. Carolan et al. 2021; J. Varela et al. 2022a; S. Gupta et al. 2023). Previous studies show that the interplay of stellar winds and CMEs with planetary magnetic-field strength and configurations controls both the magnitude and location of atmospheric escape (J. D. Alvarado-Gómez et al. 2022; O. Cohen et al. 2022; A. Presa et al. 2024). Our results complement these works by highlighting that during stellar wind and CME forcing on magnetized planets, both the nightside magnetotail and cusp regions are critical avenues for atmospheric loss.

4. Conclusions

In this study, we employ 3D global MHD modeling to investigate how the magnetic orientations of stellar wind and ICME magnetic fields impact (exo)planetary environments.



(B) Massloss rate across all six planes

Figure 4. (Continued.)

Through simulations, we explore atmospheric escape rates, global magnetospheric polarity dynamics, and magnetotail current density evolution across planets with varying magnetic-field strengths, ranging from unmagnetized to magnetized (exo)planets.

For unmagnetized planets, we find that the mass-loss rate does not strongly depend on the stellar wind and stellar CME magnetic-field orientation. As an ICME impacts the planet, there is a compression in the planetary magnetosphere, leading to a momentarily dip in the atmospheric mass-loss rates. After the compression, the ICME passage leads to substantially higher atmospheric escape rates than nominal stellar wind conditions. In the case of a magnetized planet, when the planetary and stellar wind magnetic fields are aligned in the same direction, the planetary magnetosphere provides shielding against atmospheric escape compared to an unmagnetized planet, which is expected. Intrinsic planetary magnetic fields, however, do not always protect the planet against atmospheric escape. It can lead to enhanced mass loss, in some cases depending upon the orientation of the stellar wind magnetic field.

Most notably, our simulations show that unmagnetized planets undergo global magnetic polarity reversals when the stellar wind magnetic field or stellar CME orientation reverses relative to the preexisting ambient IMF conditions. This polarity reversal phenomena becomes less pronounced with

increasing planetary magnetic-field strength. These theoretical findings are supported by previous observational studies—such as those gleaned from Venus—which exhibit global polarity reversals under similar conditions.

We analyze the current density magnitude near the planet at the magnetotail side. Our results show that during polarity reversals, the current density magnitude temporarily drops for the case of an unmagnetized planet. For the magnetized planet, the current density magnitude is higher for impacts of ICMEs with opposite magnetic-field orientation with respect to the planetary magnetic field. This is likely due to reconnection dynamics dominating the star–planet interactions in this case. We speculate that the observation of a drop in heavy-ion flux in the magnetotail during polarity reversals in the Venusian environment (D. Vech et al. 2016) is due to this drop in current density (which is manifested in our simulations for an unmagnetized planet).

Our findings have important implications for distinguishing between unmagnetized and magnetized planets and for devising future observational strategies for constraining (exo) planetary magnetism. Furthermore, insights on atmospheric dynamics forced by stellar plasma winds and magnetic storms gleaned from our simulations have relevance for characterizing habitability of (exo)planets from the perspective of star–planet interactions mediated via magnetic fields.

We have chosen a grid resolution that balances numerical accuracy with feasibility based on computational resources given the high computational cost of such simulations. To check the robustness of our primary conclusions, we have tested the sensitivity of our results to higher grid resolution. As discussed in Appendix A, increasing the resolution does not change the key qualitative dynamics exhibited in our simulations, and our main conclusions regarding stellar magnetic storm forced polarity reversal of unmagnetized or weakly magnetized (exo)planets remain unaffected. There are some quantitative changes in the computed atmospheric mass-loss rates and magnetotail current densities; however, the large-scale magnetospheric topology, the relative enhancement of magnetotail currents for southward ICME driving, and the relative ordering of escape rates across different IMF-ICME configurations are robust to further increase in resolution.

Our study is relevant for explorations of Earth-like, far-out rocky exoplanets around a Sun-like star. The motivation for this specific study stems from the fact that the Earth is the only planet known to host life. Close-in, hot Jupiters, although observed more easily, are not likely to be habitable. Young solar analogs, active rapidly rotating stars, and M dwarf stars can drive stellar winds with mass-loss rates that are 1 to several orders of magnitude higher than solar values and may produce CMEs with magnetic-field strengths and velocities substantially exceeding those considered in the present study, for which the Sun has been used as a template. Under such extreme stellar forcing, the interplay between the external magnetic pressure associated with the stellar wind or CME, the intrinsic planetary dipole pressure, and magnetic reconnection dynamics may change significantly; under stronger stellar forcing conditions, we surmise that polarity reversal timescales would be shorter, and even planets with stronger magnetic fields relative to Earth may undergo polarity reversals under extreme CME forcing. The differential response of induced and intrinsic magnetospheres to CME forcing discussed here for near-Earth solar-wind conditions may, therefore, become even more pronounced in extreme stellar environments.

Given that a major impetus for exoplanetary exploration is the search for habitable planets beyond the solar system, we deem this to be a reasonable approach from the intellectual perspective. While we appreciate that immediate observational tests may not be possible, future observations have a strong potential to uncover such systems, and we believe our work lays the theoretical foundations or paradigm of one of the possible methods for detecting exoplanetary magnetic fields.

Acknowledgments

The development of the Storm Interaction module (CESSI-STORMI) and the simulations were carried out at the Center of Excellence in Space Sciences India (CESSI), supported by IISER Kolkata, Ministry of Education, Government of India. We gratefully thank the Santimay and Sunanda Basu Foundation for enabling the computational infrastructure used in this study via the Sunanda and Santimay Basu Space Weather Computational Cluster. We also acknowledge the use of the high-performance computing facility Pegasus at IUCAA for this work. S.G. expresses her gratitude to Dr. Jagannath Nayak, Director CHESS, and Saumendra Nath Datta, Technology Director at CHESS, for the necessary approval and encouragement to continue her PhD thesis research work at CESSI. We acknowledge Dr. Antoine Strugarek of CEA Saclay and Dr Arnab Basak for useful discussions. S.R. thanks Roger Varney for the support. We also acknowledge useful and constructive comments by the anonymous referee.

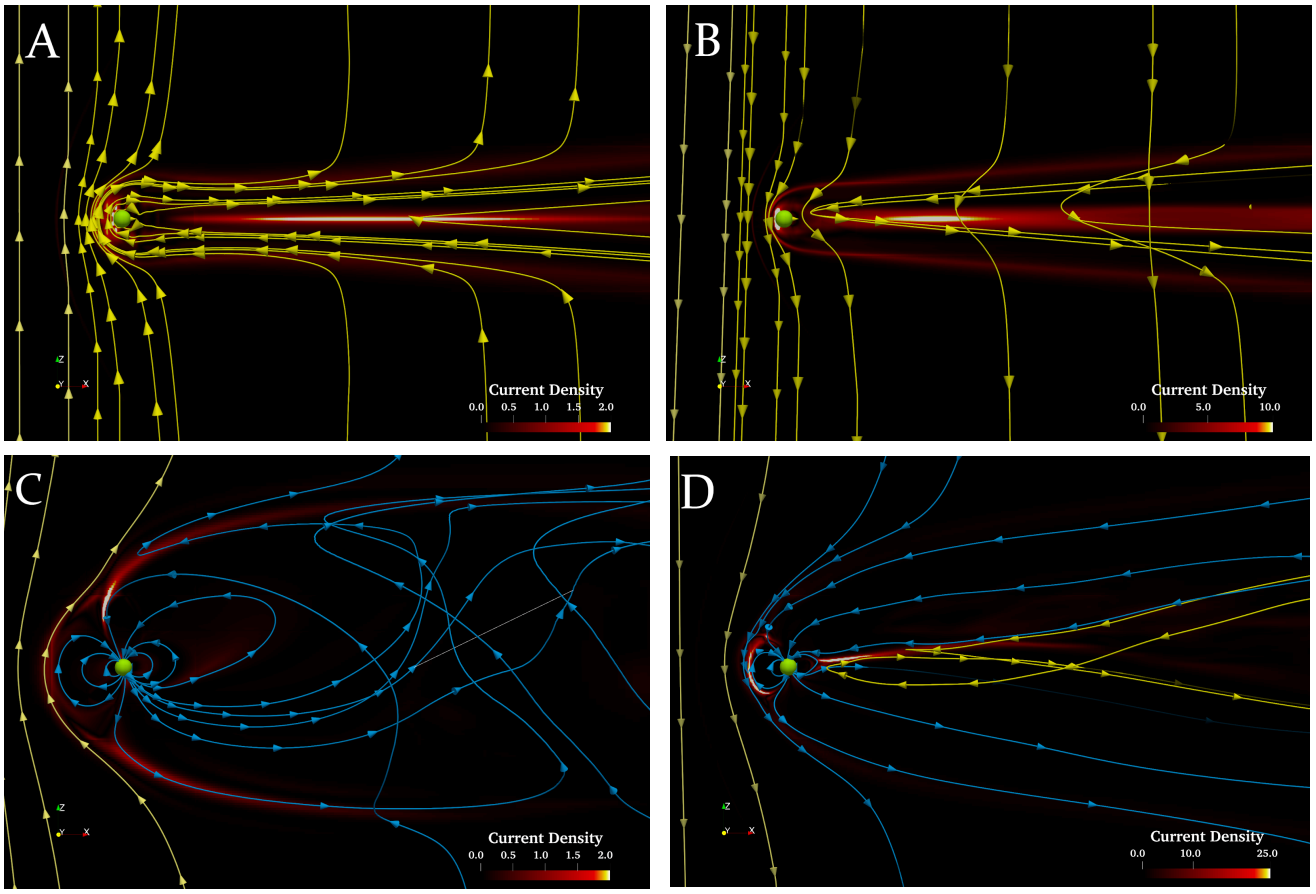
Data Availability

All simulation runs in this study are performed using the STORM Interaction Module (CESSI-STORMI), which was developed based on the open-source 3D MHD PLUTO code. Data from our simulations will be shared upon reasonable request to the corresponding author.

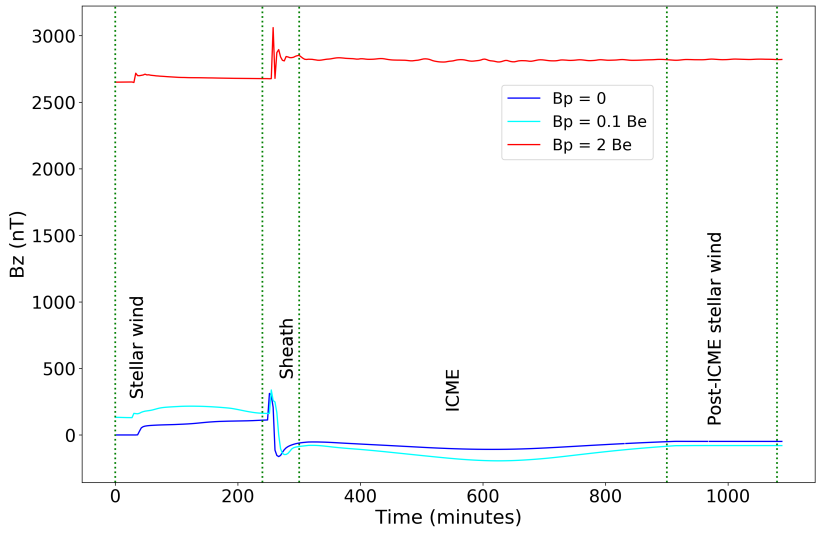
Appendix A
Impact of Grid Resolution on Results

Global MHD simulations of star–planet interactions involve a trade-off between resolving small-scale current dynamics and covering the large spatial domains needed to capture global magnetospheric structure. In this work, we refer to the original simulations described in Section 2 as our *baseline simulations*. These runs resolve the planetary environment and magnetotail sufficiently to explore large-scale trends in magnetic topology, magnetotail current sheets, and relative changes in mass loss. A large number of high-resolution runs over such large spatially extended domains are computationally very expensive. Nevertheless, to explore the influence of grid resolution on our main conclusions, we have carried out a set of higher-resolution simulations for a representative subset of cases.

In these high-resolution simulations, the central region extending from $-5\ R_p$ to $+5\ R_p$ is resolved with 100 grid cells in each direction. The regions from $-10\ R_p$ to $-5\ R_p$ and from $+5\ R_p$ to $+10\ R_p$ are each resolved with 30 grid cells. The intervals from $-25\ R_p$ to $-10\ R_p$ and from $+10\ R_p$ to $+25\ R_p$ use 45 grid cells, while the regions from $-50\ R_p$ to $-25\ R_p$, $+25\ R_p$ to $+50\ R_p$, -50 to $-100\ R_p$ and 50 to $100\ R_p$ are resolved with 50 grid cells. Beyond $\pm 100\ R_p$, the grid spacing



(a)



(b)

Figure A1. (a) Polarity reversal in (exo)planetary magnetospheres for high-resolution simulations: (A) steady-state configuration when northward stellar wind interacts with unmagnetized planet (t = 121.6 minutes); (B) magnetospheric configuration during southward-oriented ICME interaction (t = 317.68 minutes). Panels (C) and (D) show a similar interaction for magnetized planet ($B_p = 2B_e$). (b) z-component of magnetic field at 2.8 R_p on the planetary dayside for high-resolution runs.

is coarsened such that each additional interval of 2 R_p is represented by a single grid cell. To validate that our grid resolution is adequate and does not introduce numerical artifacts, we conducted a divergence error analysis by evaluating the characteristic error length scale, $B/\nabla \cdot \boldsymbol{B}$. Our analysis confirms robust global and regional stability,

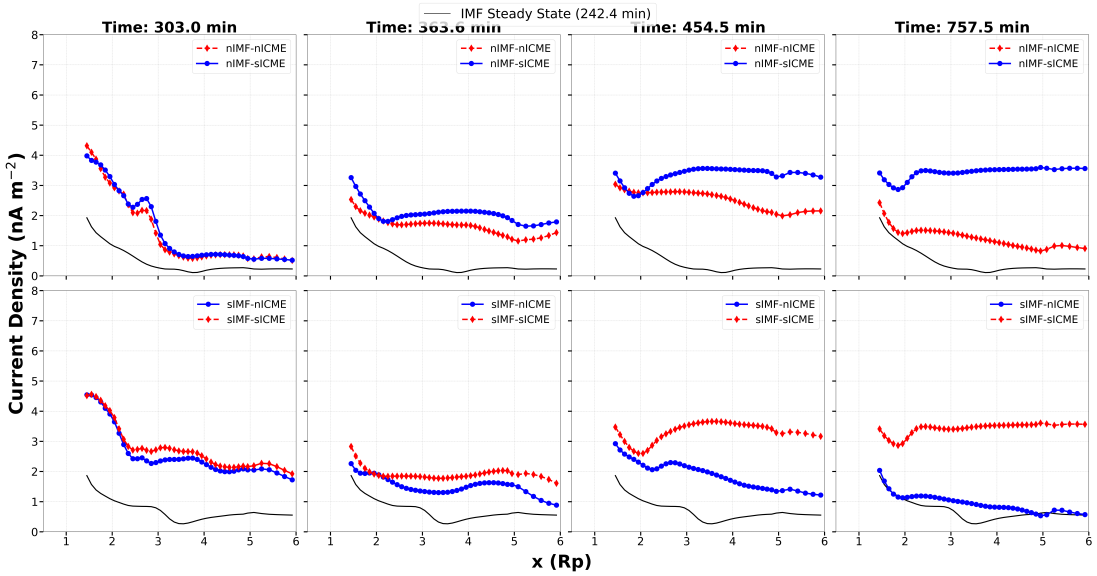


Figure A2. Magnetotail current density evolution for $B_p = 0.1B_e$ for high-resolution runs.

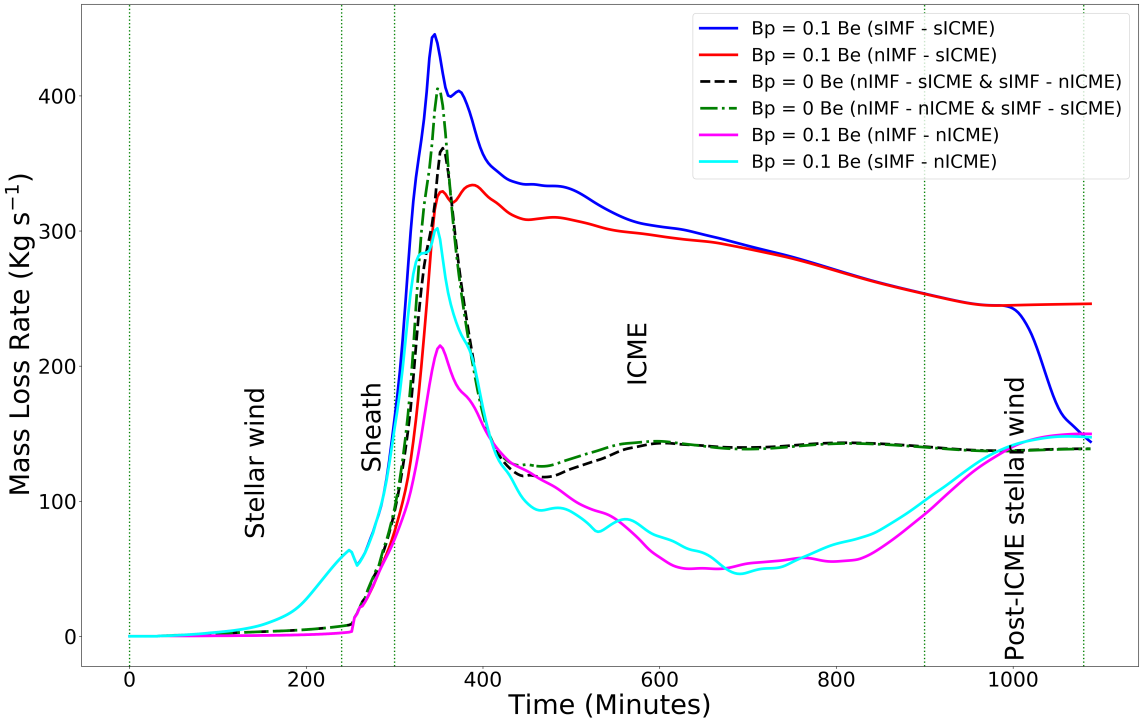


Figure A3. Temporal evolution of atmospheric mass-loss rates for unmagnetized and magnetized (exo)planets for high-resolution runs.

ensuring that numerical monopoles do not impact the overall magnetic topology.

Figure A1(a) depicts the global magnetospheric configuration for the cases shown in Figure 2 of the baseline simulations. Panels (A) and (B) of Figure A1 show the magnetospheric configurations for the unmagnetized planet. The plots show the global polarity reversal when transitioning from northward nominal stellar wind to southward ICME. Panels (C) and (D) show the same magnetospheric configurations for $B_p = 2\ B_e$, demonstrating that the polarity does not reverse in the vicinity of the planet. Figure A1(b) shows the dayside magnetic polarity at 2.8 R_p for three planetary magnetic-field strengths, $B_p = 0$, $0.1B_e$, and $2B_e$, in the high-resolution configuration. The unmagnetized and weakly magnetized cases still exhibit a reversal of the dayside field in response to changes in the external field orientation, whereas the strongly magnetized planet maintains its intrinsic polarity in the near-planet region. Although the precise transition radius and profile sharpness vary slightly, the qualitative distinction between induced and intrinsic magnetospheric responses remain unchanged, reinforcing our conclusions.

Figure A2 presents the magnetotail current density magnitude for the $B_p = 0.1B_e$ case, computed in the same nightside region as in the baseline simulations. The peak current density is reduced at higher resolution. However, the relative behavior remains the same; intervals with southward-oriented ICMEs still exhibit enhanced magnetotail current density compared to northward ICME configurations, and the temporal evolution follows the same pattern as in the baseline runs. This indicates that while the quantitative amplitudes of current density are resolution-dependent, the qualitative trends are robust.

Figure A3 shows the atmospheric mass-loss rates for the high-resolution $B_p = 0$ and $B_p = 0.1\ B_e$ cases. The absolute values of the mass-loss rate are lower than in the baseline simulations—implying a more confined interaction region at higher resolution. Nonetheless, the qualitative behavior is preserved; cases with southward-oriented ICMEs have higher mass-loss rates than their northward counterparts, and configurations in which the stellar wind magnetic field is aligned with the planetary dipole (both northward) exhibit reduced mass loss compared to the unmagnetized case. The characteristic initial dip during magnetospheric compression, followed by an enhanced loss phase during the ICME passage, is also apparent in the high-resolution runs.

The high-resolution simulations show that while the quantitative values of atmospheric mass-loss rate and magnetotail current density may vary slightly with resolution, the qualitative behavior of these star–planet interactions and the underlying physical conclusions remain robust.

Appendix B
Additional Simulations of the Polarity Reversal Transition

To further investigate the polarity-reversing magnetospheric behavior, we performed additional simulations with intermediate planetary magnetic-field strengths of $B_p = 0.3B_e$ and $B_p = 0.5B_e$ while keeping the stellar wind and ICME parameters unchanged. The results indicate that the susceptibility to CME-driven polarity reversal decreases progressively with increasing intrinsic planetary magnetic-field strength. As shown in Figure B1, planets with the $B_p = 0.3B_e$ case experience substantial weakening and reconfiguration of the dayside magnetic field. For $B_p = 0.5B_e$, the intrinsic dipolar topology remains largely preserved during the reversal of the external stellar magnetic field.

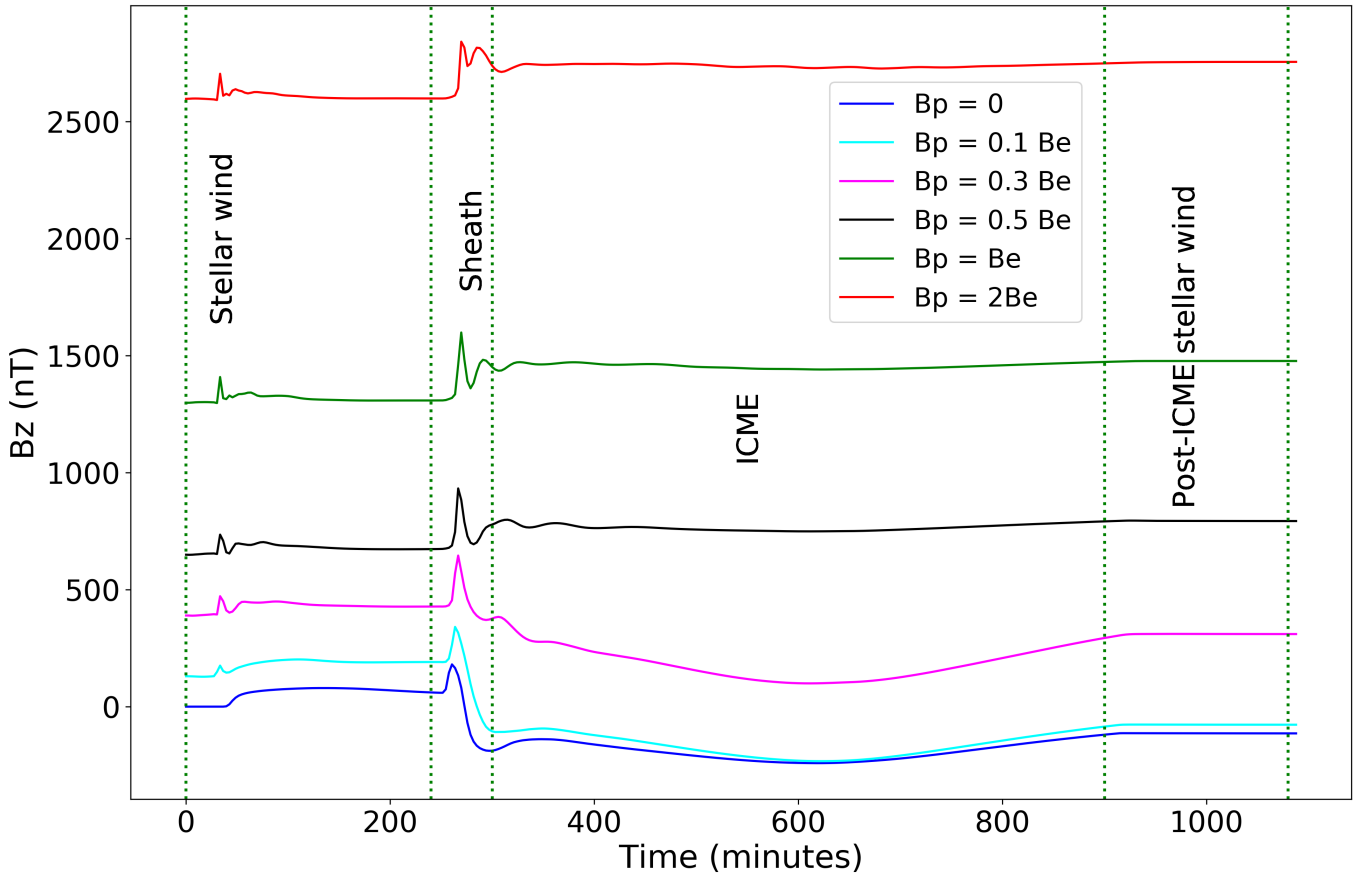


Figure B1. Temporal evolution of the dayside magnetic-field component B_z measured at $2.8R_p$. The additional simulations ($B_p = 0.3\ B_e$ and $0.5\ B_e$) show a gradual transition from induced to intrinsic magnetospheric behavior, with increasing planetary magnetic-field strength progressively suppressing CME-driven polarity reversals.

ORCID iDs

Sakshi Gupta https://orcid.org/0000-0002-8920-1495
Souvik Roy https://orcid.org/0000-0002-0471-4591
Dibyendu Nandy https://orcid.org/0000-0001-5205-2302

References

Alvarado-Gómez, J. D., Cohen, O., Drake, J. J., et al. 2022, ApJ, 928, 147
Alvarado-Gómez, J. D., Hussain, G. A. J., Cohen, O., et al. 2016, A&A, 594, A95
Argiroffi, C., Reale, F., Drake, J. J., et al. 2019, NatAs, 3, 742
Baker, D. N., Pulkkinen, T. I., Li, X., et al. 1998, GeoRL, 25, 2975
Baruah, Y., Roy, S., Sinha, S., et al. 2024, SpWea, 22, e2023SW003716
Basak, A., & Nandy, D. 2021, MNRAS, 502, 3569
Bastian, T. S., Dulk, G. A., & Leblanc, Y. 2000, ApJ, 545, 1058
Benna, M., Acuña, M. H., Anderson, B. J., et al. 2009, GeoRL, 36, L04109
Bothmer, V., & Schwenn, R. 1998, AnGeo, 16, 1
Burkhart, G. R., Drake, J. F., & Chen, J. 1990, JGRA, 95, 18833
Burton, R. K., McPherron, R. L., & Russell, C. T. 1975, JGR, 80, 4204
Carolan, S., Vidotto, A. A., Hazra, G., Villarreal D'Angelo, C., & Kubyshkina, D. 2021, MNRAS, 508, 6001
Chen, P. F. 2011, LRSP, 8, 1
Cherenkov, A., Bisikalo, D., Fossati, L., & Möstl, C. 2017, ApJ, 846, 31
Cohen, O., Alvarado-Gómez, J. D., Drake, J. J., et al. 2022, ApJ, 934, 189
Cohen, O., Drake, J. J., Glocer, A., et al. 2014, ApJ, 790, 57
Cohen, O., Garraffo, C., Moschou, S.-P., et al. 2020, ApJ, 897, 101
Cohen, O., Ma, Y., Drake, J. J., et al. 2015, ApJ, 806, 41
Connerney, J. E. P., Kotsiaros, S., Oliversen, R. J., et al. 2018, GeoRL, 45, 2590
Daglis, I. A., Chang, L. C., Dasso, S., et al. 2021, AnGeo, 39, 1013
Das, S. B., Basak, A., Nandy, D., & Vaidya, B. 2019, ApJ, 877, 80
Davenport, J. R. A. 2016, ApJ, 829, 23
DiBraccio, G. A., Espley, J. R., Gruesbeck, J. R., et al. 2015, GeoRL, 42, 8828
Dubinin, E., Barabash, S., Fedorov, A., et al. 2013a, SSRv, 175, 179
Dubinin, E., Fraenz, M., Woch, J., et al. 2012, GeoRL, 39, L01104
Dubinin, E., Fraenz, M., Zhang, T. L., et al. 2013b, JGRA, 118, 7624
Dungey, J. W. 1961, PhRvL, 6, 47
Egan, H., Jarvinen, R., Ma, Y., & Brain, D. 2019, MNRAS, 488, 2108
Fear, R. C., Coxon, J. C., & Jackman, C. M. 2019, GeoRL, 46, 14239
Fortney, J. J., Dawson, R. I., & Komacek, T. D. 2021, JGRE, 126, e2020JE006629
Futaana, Y., Stenberg Wieser, G., Barabash, S., & Luhmann, J. G. 2017, SSRv, 212, 1453
Gallet, F., Charbonnel, C., Amard, L., et al. 2017, A&A, 597, A14
Gold, T., & Hoyle, F. 1960, MNRAS, 120, 89
Gonzalez, W. D., Joselyn, J. A., Kamide, Y., et al. 1994, JGRA, 99, 5771
Gonzalez, W. D., Tsurutani, B. T., & Clúa de Gonzalez, A. L. 1999, SSRv, 88, 529
Good, S., & Forsyth, R. 2016, SoPh, 291, 239
Gosling, J. T. 1993, JGRA, 98, 18937
Grießmeier, J.-M., Zarka, P., & Spreeuw, H. 2007, A&A, 475, 359
Gunell, H., Maggiolo, R., Nilsson, H., et al. 2018, A&A, 614, L3
Günther, M. N., Zhan, Z., Seager, S., et al. 2020, AJ, 159, 60
Gupta, S., Basak, A., & Nandy, D. 2023, ApJ, 953, 70
Hallinan, G., Antonova, A., Doyle, J. G., et al. 2008, ApJ, 684, 644
Hazra, G., Vidotto, A. A., Carolan, S., D'Angelo, C. V., & Fionnagáin, D. Ó. 2024a, MNRAS, 536, 1089
Hazra, G., Vidotto, A. A., Carolan, S., Villarreal D'Angelo, C., & Fionnagáin, D. 2024b, MNRAS, 536, 1089
Hu, Q., Qiu, J., Dasgupta, B., Khare, A., & Webb, G. M. 2014, ApJ, 793, 53
Hundhausen, A. 1999, in The Many Faces of the Sun: A Summary of the Results from NASA's Solar Maximum Mission, ed. K. T. Strong et al. (Springer), 143
Inoue, S., Maehara, H., Notsu, Y., et al. 2023, ApJ, 948, 9
Jakosky, B. M., & Phillips, R. J. 2001, Natur, 412, 237
Janvier, M., Winslow, R. M., Good, S., et al. 2019, JGRA, 124, 812
Jia, Y.-D., Combi, M. R., Hansen, K. C., & Gombosi, T. I. 2007, JGRA, 112, A05223
Jia, Y. D., Russell, C. T., Jian, L. K., et al. 2009, ApJL, 696, L56
Jolitz, R. D., Rahmati, A., Brain, D. A., et al. 2023, JGRA, 128, e2022JA030884
Khodachenko, M. L., Sasunov, Y., Arkhypov, O. V., et al. 2014, IAUS, 300, 335
Kislyakova, K. G., Holmström, M., Odert, P., et al. 2019, A&A, 623, A131
Komar, C. M., Cassak, P. A., Dorelli, J. C., Glocer, A., & Kuznetsova, M. M. 2013, JGRA, 118, 4998
Kowalski, A. F., Hawley, S. L., Wisniewski, J. P., et al. 2013, ApJS, 207, 15
Kurth, W. S., Gurnett, D. A., & Bolton, S. J. 2016, JGRA, 121, 4608
Lammer, H., Kasting, J. F., Chassefière, E., et al. 2008, SSRv, 139, 399
Lammer, H., Selsis, F., Ribas, I., et al. 2003, ApJL, 598, L121
Lamy, L., Zarka, P., Cecconi, B., et al. 2017, Sci, 318, 743
Li, G., Lu, H., Cao, J., Li, Y., & Li, S. 2023, A&A, 673, A3
Luhmann, J. G., Russell, C. T., Zhang, M., & Schunk, R. W. 1992, GeoRL, 19, 1217
Lynch, C. R., Murphy, T., Kaplan, D. L., Ireland, M., & Bell, M. E. 2018, MNRAS, 481, 5000
Ma, Y. J., Nagy, A. F., Russell, C. T., et al. 2013, JGRA, 118, 321
Masters, A. 2012, JGRA, 117, A06213
McPherron, R. L., Weygand, J. M., & Hsu, T.-S. 2008, JASTP, 70, 303
Mignone, A., Bodo, G., Massaglia, S., et al. 2007, ApJS, 170, 228
Milan, S. E., Carter, J. A., Sangha, H., Bower, G. E., & Anderson, B. J. 2021, JGRA, 126, e2020JA028437
Mulligan, T., Russell, C. T., & Luhmann, J. G. 1998, GeoRL, 25, 2959
Murphy, T., Bell, M. E., Kaplan, D. L., et al. 2015, MNRAS, 446, 2560
Namekata, K., Maehara, H., Honda, S., et al. 2022, 44th COSPAR Scientific Assembly, 44, 2446
Namekata, K., Maehara, H., Notsu, Y., et al. 2025, ApJ, 993, 80
Nandy, D. 2004, SoPh, 224, 161
Nandy, D., Baruah, Y., Bhowmik, P., et al. 2023, JASTP, 248, 106081
Nandy, D., & Martens, P. 2007, AdSpR, 40, 891
Odert, P., Leitzinger, M., Hanslmeier, A., & Lammer, H. 2017, MNRAS, 472, 876
Pal, S., Nandy, D., & Kilpua, E. K. J. 2022, A&A, 665, A110
Palmerio, E., Kilpua, E. K. J., Möstl, C., et al. 2018, SpWea, 16, 442
Paschmann, G., Sckopke, N., Russell, C. T., et al. 1979, Natur, 282, 243
Paul, A., Strugarek, A., & Vaidya, B. 2023, JGRA, 128, e2023JA031718
Presa, A., Driessen, F. A., & Vidotto, A. A. 2024, MNRAS, 534, 3622
Preusse, S., Kopp, A., Büchner, J., & Motschmann, U. 2007, P&SS, 55, 589
Pulkkinen, T. 2007, LRSP, 4, 1
Raeder, J. 1999, JGRA, 104, 17357
Ramstad, R., Barabash, S., Futaana, Y., Nilsson, H., & Holmström, M. 2018, JGRE, 123, 3051
Rodríguez-Mozos, J. M., & Moya, A. 2019, A&A, 630, A52
Roy, S., & Nandy, D. 2023, ApJL, 950, L11
Russell, C., Luhmann, J., & Strangeway, R. 2006, P&SS, 54, 1482
Russell, C. T. 2001, P&SS, 49, 1005
Schwenn, R. 2006, LRSP, 3, 2
Seidel, J. V., Parmentier, V., Prinoth, B., et al. 2026, NatAs, 10, 1145
Shaikhislamov, I. F., Khodachenko, M. L., Lammer, H., et al. 2016, ApJ, 832, 173
Slavin, J. A., Schwingenschuh, K., Riedler, W., & Yeroshenko, Y. 1991, JGRA, 96, 11235
Smith, A. M. S., Cameron, A. C., Greaves, J., et al. 2009, MNRAS, 395, 335
Sonnerup, B. U. O. 1974, JGR, 79, 1546
Tang, B. B., Guo, X. C., Wang, C., Hu, Y. Q., & Kan, J. R. 2009, JGRA, 114, A08203
Trotignon, J., Grard, R., & Skalsky, A. 1993, P&SS, 41, 189
Turner, J. D., Zarka, P., Grießmeier, J.-M., et al. 2021, A&A, 645, A59
Turnpenney, S., Nichols, J. D., Wynn, G. A., & Jia, X. 2020, MNRAS, 494, 5044
Varela, J., Brun, A. S., Strugarek, A., et al. 2022a, A&A, 659, A10
Varela, J., Brun, A. S., Zarka, P., et al. 2022b, SpWea, 20, e2022SW003164
Vech, D., Stenberg, G., Nilsson, H., et al. 2016, JGRA, 121, 3951
Veronig, A. M., Dissauer, K., Kliem, B., et al. 2025, LRSP, 22, 2
Vidotto, A. A., & Cleary, A. 2020, MNRAS, 494, 2417
Vidotto, A. A., Fares, R., Jardine, M., Moutou, C., & Donati, J.-F. 2015, MNRAS, 449, 4117
Vignes, D., Mazelle, C., Rme, H., et al. 2000, GeoRL, 27, 49
Wang, C., Han, J. P., Li, H., Peng, Z., & Richardson, J. D. 2014, JGRA, 119, 6199
Wang, L., Huang, C., Du, A., et al. 2023, GeoRL, 50, e2023GL104996
Way, M. J., & Del Genio, A. D. 2020, JGRE, 125, e2019JE006276
Wood, B. E., Müller, H.-R., Redfield, S., et al. 2021, ApJ, 915, 37
Xu, S., Mitchell, D. L., Weber, T., et al. 2020, JGRA, 125, e2019JA027755
Yang, H., & Liu, J. 2019, ApJS, 241, 29
Zarka, P. 1998, JGRE, 103, 20159
Zarka, P. 2007, P&SS, 55, 598
Zhang, T. L., Delva, M., Baumjohann, W., et al. 2008, JGRE, 113, E00B20
Zong, Q. 2022, AnGeo, 40, 121